

Algebraic reconstruction for 3D magnetic resonance–electrical impedance tomography (MREIT) using one component of magnetic flux density

Y Ziya İder and Serkan Onart

Department of Electrical and Electronics Engineering, Bilkent University, Ankara, Turkey

E-mail: ider@ee.bilkent.edu.tr

Received 21 August 2003, accepted for publication 28 November 2003

Published 3 February 2004

Online at stacks.iop.org/PM/25/281 (DOI: 10.1088/0967-3334/25/1/032)

Abstract

Magnetic resonance–electrical impedance tomography (MREIT) algorithms fall into two categories: those utilizing internal current density and those utilizing only one component of measured magnetic flux density. The latter group of algorithms have the advantage that the object does not have to be rotated in the magnetic resonance imaging (MRI) system. A new algorithm which uses only one component of measured magnetic flux density is developed. In this method, the imaging problem is formulated as the solution of a non-linear matrix equation which is solved iteratively to reconstruct resistivity. Numerical simulations are performed to test the algorithm both for noise-free and noisy cases. The uniqueness of the solution is monitored by looking at the singular value behavior of the matrix and it is shown that at least two current injection profiles are necessary. The method is also modified to handle region-of-interest reconstructions. In particular it is shown that, if the image of a certain xy -slice is sought for, then it suffices to measure the z -component of magnetic flux density up to a distance above and below that slice. The method is robust and has good convergence behavior for the simulation phantoms used.

Keywords: magnetic resonance–electrical impedance tomography, MREIT, B_z based algorithm, EIT, finite element method

1. Introduction

Magnetic resonance–electrical impedance tomography (MREIT) reconstruction algorithms fall into two categories: those utilizing internal current density information and those utilizing only one component of measured magnetic flux density (Birgöl *et al* 2003b). The main disadvantage of the former group of algorithms is that in order to calculate the internal current

density distribution from Ampère's law, one has to measure all three components of magnetic flux density. This requires rotation of the object because using magnetic resonance imaging (MRI), one can measure only one component of magnetic flux density at a time.

Several algorithms have been proposed which utilize only one component of magnetic flux density, namely B_z , where z is the direction of the main magnetic field of the MR system. Birgül and İder (1995), İder and Birgül (1998) and Birgül *et al* (2003b) use an iterative sensitivity matrix method which utilizes the linearized relation between perturbation in B_z and perturbation in conductivity. Seo *et al* (2003a) use the gradient of B_z , i.e. ∇B_z , to reconstruct the internal current density distribution in axially symmetric cylindrical sections, after which they use a J-substitution algorithm (Kwon *et al* 2002, Khang *et al* 2002) to reconstruct conductivity. Seo *et al* (2003b) and Oh *et al* (2003) have developed iterative algorithms which utilize the Laplacian of B_z , i.e. $\nabla^2 B_z$. In these iterative algorithms, at each iteration the gradient of conductivity is found first. Seo *et al* (2003b) integrate this gradient on Cartesian lines to reconstruct conductivity. Oh *et al* (2003), on the other hand, use a layer potential technique to reconstruct conductivity from its gradient.

The new reconstruction algorithm presented in this study formulates image reconstruction as the iterative solution of a non-linear matrix equation. The formulation used in this study also provides a handle for monitoring the uniqueness of the solution. İder *et al* (2003) have analyzed uniqueness and reconstruction in MREIT and have proposed three methods for numerical implementation provided that the internal current density is known. This paper extends one of the methods given in İder *et al* (2003) to the problem of reconstruction using only one component of magnetic flux density. Preliminary results of this work are presented by Onart and İder (2003).

In the following, first, the formulation and numerical solution of the forward problem is explained. Then, the inverse problem is formulated and numerical methods for its solution are presented. Finally, simulation results which cover uniqueness considerations, region-of-interest reconstructions and reconstruction in the presence of noise are given.

2. Formulation and solution of the forward problem

Let Ω be a bounded and electrically conductive domain in \mathbb{R}^3 with boundary Γ . Conductivity and resistivity distributions inside Ω are σ and ρ , respectively, both assumed to be positive. We also attach surface electrodes on Γ to inject current into Ω . Potential distribution Φ obeys Laplace's equation and Neumann boundary conditions as follows:

$$\begin{cases} \nabla \cdot (\sigma \nabla \Phi) = 0 & \text{in } \Omega \\ -\sigma \nabla \Phi \cdot \mathbf{n} = \mathbf{J}_{\text{inj}} & \text{on } \Gamma \end{cases} \quad (1)$$

where \mathbf{n} is the unit outward normal vector and \mathbf{J}_{inj} is the injected surface current density which is non-zero only on current injection electrodes. Φ , current density, \mathbf{J} and electric field, \mathbf{E} , are related in Ω by

$$\mathbf{J} = \sigma \mathbf{E} = -\sigma \nabla \Phi. \quad (2)$$

Magnetic flux density \mathbf{B} , due to \mathbf{J} , is given by the Biot–Savart integral

$$\mathbf{B}(\mathbf{r}) = \frac{\mu_0}{4\pi} \int_{\Omega} \mathbf{J}(\mathbf{r}') \times \frac{\mathbf{r} - \mathbf{r}'}{|\mathbf{r} - \mathbf{r}'|^3} dv' \quad (3)$$

where \mathbf{r} and \mathbf{r}' are field and source vectors defined in Ω .

The finite element method (FEM) is used to solve equation (1). In simulation studies, a rectangular prism object as shown in figure 1 is divided into small hexahedral (cubic) constant

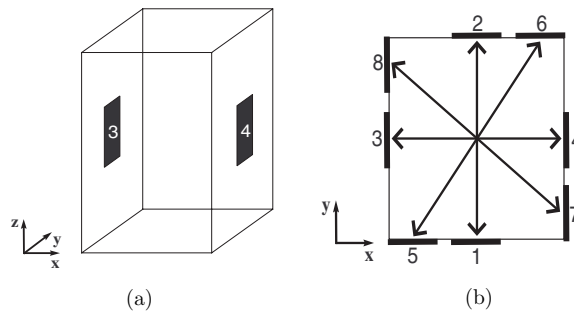


Figure 1. (a) Rectangular prism object used in simulations. Only electrodes 3 and 4 are shown on the rectangular prism. (b) All electrodes shown on the mid-horizontal cross section of the prism. All electrodes are of the same size and shape. Double ended arrows denote the pairs of electrodes used to inject current.

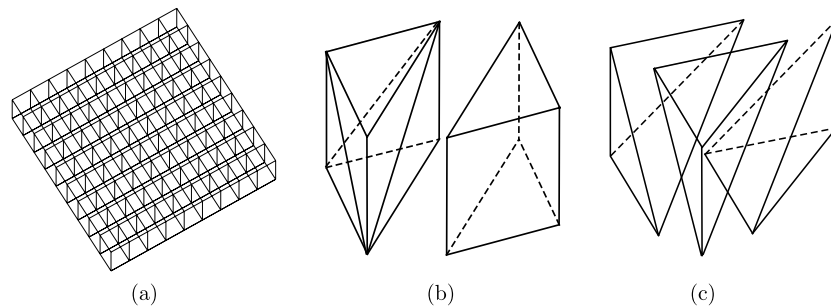


Figure 2. Elements used in FEM. (a) Square Cartesian mesh, made of cubic hexahedrons, for an xy -slice of the rectangular prism object (b) Two pentahedrons forming a hexahedron (c) Three tetrahedrons forming a pentahedron.

conductivity elements using a regular Cartesian mesh. In figure 2 the elements used in FEM are shown. Each hexahedron is divided into two pentahedrons and each pentahedron, in turn, is divided into three tetrahedrons. In a tetrahedral element Φ is approximated by a first-order polynomial with respect to the coordinate axes (Silvester and Ferrari 1996), and therefore each tetrahedron has constant \mathbf{E} and \mathbf{J} in it. In assigning \mathbf{E} and \mathbf{J} values to a hexahedron, we averaged the corresponding values of the six tetrahedrons encompassed by that hexahedron.

Magnetic flux density is calculated by discretizing equation (3) such that each tetrahedron acts as a current source located at its center of gravity, and field points are at the hexahedron centers. For uniform current density and uniform conductivity distribution in a rectangular 3D object, Biot–Savart integral is evaluated semi-analytically and compared with numerical results to understand the amount of error introduced due to this approximation. For semi-analytical evaluation, the triple integral in equation (3) is handled as follows: integration w.r.t. x' and y' variables is first evaluated analytically using symbolic math tools of MATLAB. The remaining integral w.r.t. z' variable is calculated numerically by adaptive Simpson quadrature to a relative tolerance of 10^{-7} (Hanselman and Littlefield 2001). Maximum and mean absolute differences in magnetic flux densities calculated by the semi-analytical method and our numerical procedure are found to be 2.5% and 0.055%, respectively. The relative L^2 difference between the two results (defined similar to equation (13)) is found to be 0.056%.

The forward problem is defined as the calculation of Φ , \mathbf{E} , \mathbf{J} and \mathbf{B} for a given conductivity distribution and for the boundary conditions defined by the current injection electrodes.

3. Formulation of the inverse problem

The inverse problem is the reconstruction of σ or ρ from the measured magnetic flux density. It has previously been shown by İder *et al* (2003), starting from $\nabla \times \mathbf{E} = 0$, that

$$\nabla R \times \mathbf{J} = -\nabla \times \mathbf{J} \quad (4)$$

where R is defined as the natural logarithm of resistivity, or equivalently $\rho = e^R$. Using the fact that $\mathbf{J} = \nabla \times \mathbf{B}/\mu_0$, and that $\nabla \times \mathbf{J} = \nabla \times (\nabla \times \mathbf{B}/\mu_0) = \nabla(\nabla \cdot \mathbf{B}/\mu_0) - \nabla^2 \mathbf{B}/\mu_0$, one obtains

$$\nabla R \times \mathbf{J} = -\nabla(\nabla \cdot \mathbf{B}/\mu_0) + \nabla^2 \mathbf{B}/\mu_0. \quad (5)$$

Since \mathbf{B} is solenoidal,

$$\nabla R \times \mathbf{J} = \nabla^2 \mathbf{B}/\mu_0. \quad (6)$$

The matrix form of this equation is

$$\begin{bmatrix} 0 & J_z & -J_y \\ -J_z & 0 & J_x \\ J_y & -J_x & 0 \end{bmatrix} \begin{bmatrix} \frac{\partial R}{\partial x} \\ \frac{\partial R}{\partial y} \\ \frac{\partial R}{\partial z} \end{bmatrix} = \frac{1}{\mu_0} \begin{bmatrix} \nabla^2 B_x \\ \nabla^2 B_y \\ \nabla^2 B_z \end{bmatrix}. \quad (7)$$

Let us now concentrate on the third row of this matrix equation, which is,

$$\frac{\partial R}{\partial x} J_y - \frac{\partial R}{\partial y} J_x = \nabla^2 B_z / \mu_0. \quad (8)$$

This equation formulates the inverse problem on slices perpendicular to the z direction. If $\nabla^2 B_z$ is measured on a constant- z slice, then the solution of this equation gives us the R distribution for that slice. Equation (8) is a first-order non-linear partial differential equation which relates the partial derivatives of R to the Laplacian of B_z/μ_0 . The non-linearity is due to the fact that the coefficients of the partial derivatives of R , i.e. J_y and J_x , are dependent on R . We used an iterative algorithm to solve equation (8), the numerical aspects of which are presented in the next section.

In general, equation (8) may not have a unique solution and therefore, as will be demonstrated in section 5, more than one current injection profiles must be used in order to obtain a unique solution for R apart from an additive constant.

4. Numerical solution of the inverse problem

To solve equation (8) numerically for a slice, we discretized it on a Cartesian mesh for which the mesh points are the hexahedron centers. Let us assume that there are $NM = N \times M$ hexahedrons in the slice of interest, where N is the number of hexahedrons in the x -direction, and M is the number of hexahedrons in the y -direction. Discretization is achieved by replacing derivatives with finite difference equivalents. The finite difference approximation can be obtained by forward, backward or central differences. On edges and corners, appropriate forward or backward differences, and in the interior regions, central difference are used. For example, also assuming that discretization steps Δx , Δy and Δz are all equal to unity, the discretized equation for the (i, j) th hexahedron, sitting in the interior part of a Cartesian mesh, i.e. $2 < i < N - 1$ and $2 < j < M - 1$, is

$$\frac{R_{(i+1,j)} - R_{(i-1,j)}}{2} J_{y(i,j)} - \frac{R_{(i,j+1)} - R_{(i,j-1)}}{2} J_{x(i,j)} = \left(\nabla^2 \frac{B_z}{\mu_0} \right)_{(i,j)} \quad (9)$$

where the discretized version of the ∇^2 operator for a scalar function U for the k th slice (not on the boundary) is

$$(\nabla^2 U)_{(i,j)} = U_{(i+1,j,k)} + U_{(i-1,j,k)} + U_{(i,j+1,k)} + U_{(i,j-1,k)} + U_{(i,j,k+1)} + U_{(i,j,k-1)} - 6U_{(i,j,k)}. \quad (10)$$

All together there are NM equations. We rearranged and combined all equations into matrix form as,

$$\mathbf{A}\mathbf{R} = \mathbf{b} \quad (11)$$

where \mathbf{A} is the $(NM \times NM)$ coefficient matrix, \mathbf{R} is the $(NM \times 1)$ vector of all hexahedron R values and \mathbf{b} is the $(NM \times 1)$ vector of $\nabla^2 B_z / \mu_0$.

Equation (11) is obtained for a single current injection profile. If there are K current injection profiles, i.e. K internal current distributions, \mathbf{J}_ℓ , renaming their \mathbf{A} matrices and \mathbf{b} vectors as \mathbf{A}_ℓ and \mathbf{b}_ℓ , where $\ell = 1, 2, \dots, K$, we obtain, by concatenation, the combined system equation

$$\mathcal{A}\mathbf{R} = \mathcal{B} \quad (12)$$

where $\mathcal{A} = [\mathbf{A}_1^T \mathbf{A}_2^T \dots \mathbf{A}_K^T]^T$ and $\mathcal{B} = [\mathbf{b}_1^T \mathbf{b}_2^T \dots \mathbf{b}_K^T]^T$.

Steps of the iterative reconstruction algorithm are then:

Step 1: Measure B_z and calculate $\nabla^2 B_z / \mu_0$ for all current profiles. Obtain \mathbf{b}_ℓ vectors for $\ell = 1, 2, \dots, K$.

Step 2: Assume an initial \mathbf{R} vector (which, for the first iteration, is considered to correspond to a uniform distribution).

Step 3: Calculate \mathbf{J}_ℓ using FEM and obtain \mathbf{A}_ℓ for $\ell = 1, 2, \dots, K$.

Step 4: Concatenate \mathbf{A}_ℓ matrices and \mathbf{b}_ℓ vectors to obtain combined system equation $\mathcal{A}\mathbf{R} = \mathcal{B}$.

Step 5: Solve the combined system equation to find \mathbf{R} .

Step 6: Stop if the stopping criterion is met. If not, go to step 3 and use the \mathbf{R} found in step 5 as the initial vector.

The solution of the combined system equation (step 5) requires that \mathcal{A} is not singular. This issue is discussed in section 5. One may check if the L^2 norm of the change of vector R between two consecutive iterations is below a preselected threshold in order to terminate the iterative algorithm. In our simulation studies we have looked at the relative L^2 error of the difference between the reconstructed image and the actual resistivity distribution in order to follow the convergence of the algorithm as iterations proceed. Relative L^2 error is defined as

$$\text{Relative } L^2 \text{ error} = 100 \frac{\|(\mathbf{r} - \mathbf{r}_{\text{org}})\|_{L^2}}{\|\mathbf{r}_{\text{org}}\|_{L^2}} \quad (13)$$

where \mathbf{r} and \mathbf{r}_{org} are the reconstructed and original (actual) resistivity vectors respectively. The i th elements of \mathbf{r} and \mathbf{R} are related by $r_i = e^{R_i}$.

5. Simulation results

Computer simulations are made to demonstrate the performance of our algorithm. Figure 1 shows the 3D conductive simulation object which is a rectangular prism with edge lengths of 32 cm, 32 cm and 64 cm for the x , y and z directions, respectively. In the same figure, current injection electrodes, numbered from 1 to 8, are also shown. For solving the forward problem using FEM for this object, we divided it into 64 slices in the z direction with 1 cm thickness each, and every slice is partitioned by a regular Cartesian mesh so that

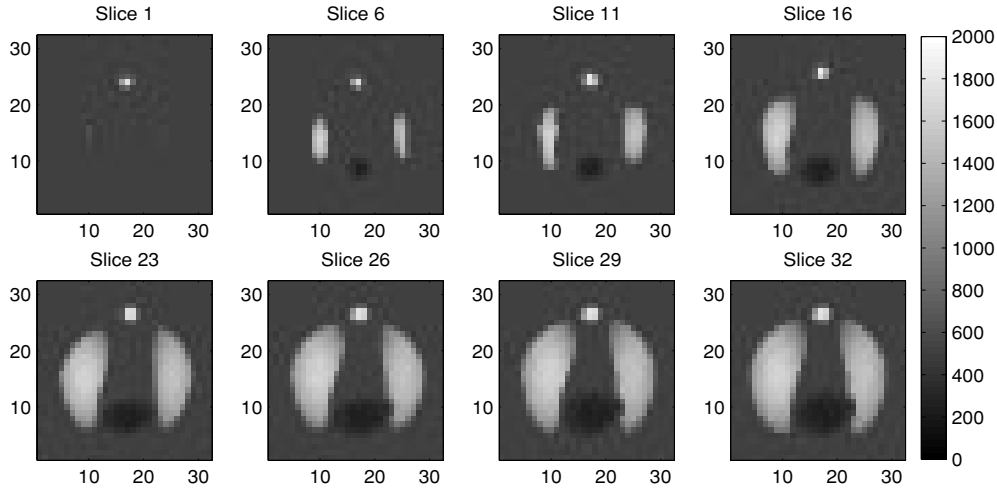


Figure 3. Resistivity distribution ρ_{org} used in simulations.

it has 32×32 hexahedrons. Therefore, one hexahedron has a volume of 1 cm^3 . Each hexahedron is assigned a uniform conductivity value. The slices are numbered from 1 to 64 starting from the bottom of the object. For example, the 10th slice is the slab between $z = 9 \text{ cm}$ and $z = 10 \text{ cm}$ planes. The object has an isotropic resistivity distribution ρ_{org} which has x , y and also z dependence, and which is also symmetric with respect to the $z = 32 \text{ cm}$ plane. Figure 3 has the resistivity distributions for nine selected slices. Background resistivity is taken as $500 \Omega \text{ cm}$. Maximum and minimum resistivity values are $1800 \Omega \text{ cm}$ and $250 \Omega \text{ cm}$, respectively.

Four current injection profiles are used. Current is injected at one time between electrodes 1–2, 3–4, 5–6 or 7–8. For each current injection profile, the z -component of magnetic flux density is calculated to generate simulated data. Electrodes cover 22 slices (22–43) in the z -direction, they are placed midway in the z -direction, and their widths are ten hexahedron sides. Therefore, each electrode is 10 cm wide and is 22 cm long in the z direction.

Figure 4 shows the logarithmic singular value plots for the combined system matrix for the first iteration of slice 32, for various current injection profile combinations. If only one current injection is used, namely with electrodes 1–2, then it is observed that the system matrix has a rank of 1011 if only the singular values larger than $(10^{-9} \times \text{maximum singular value})$ are counted. With one current injection, meaningful reconstructions are not achieved even for noise-free simulations. If two current injections are used, namely between electrodes 1–2 and 3–4, then the rank of the system becomes 1023. This shows that apart from a single degree of freedom one can reconstruct uniquely. Adding other current injections does not alter the situation and the rank of the system remains 1023. Similar behavior is observed for other slices in the region-of-interest (defined later) and also for other iterations. Obviously the combined system matrix and its singular value behavior depend on the distribution of conductivity and the imposed Neumann boundary conditions. However, by looking at the singular value behavior of the system matrix at each iteration one can at least make sure that requirement of uniqueness is not lost throughout the iterative application of the reconstruction algorithm. The reduced condition number of the combined system matrix, i.e. ratio of max singular value to the 1023rd singular value, is 3.8×10^{12} , 7041, 10 181 and 3268 for one, two, three or four current injections, respectively. The condition number is a measure of the ill-conditioning of the system matrix and indicates how tolerant the system is against measurement noise. In our

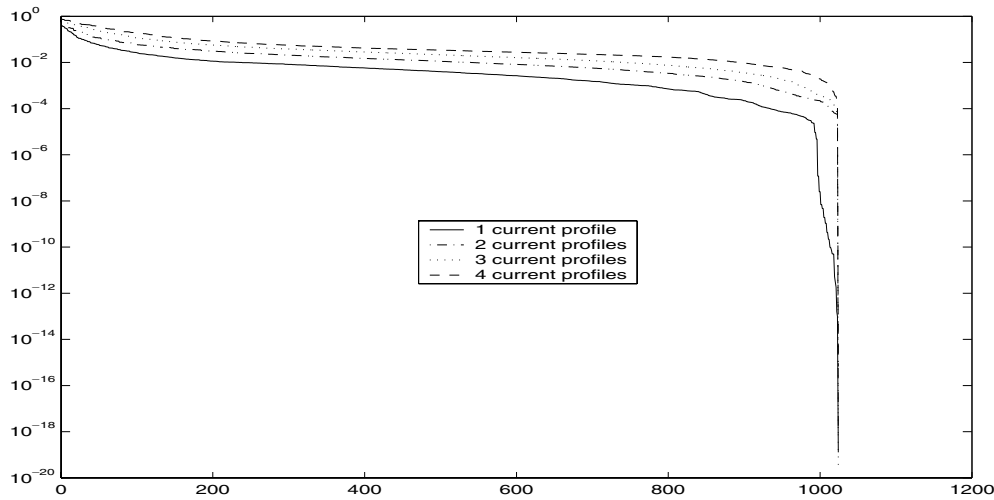


Figure 4. Singular values (logarithmic) of the combined system matrix. One current profile means current is injected between electrodes 1–2. Two current profiles mean current is injected between electrodes 1–2 and 3–4. Three current profiles means current is injected between electrodes 1–2, 3–4 and 5–6. Four current profiles mean current is injected between electrodes 1–2, 3–4, 5–6 and 7–8. The vertical axis shows the singular values normalized to the maximum singular value.

case it is apparent that more than two current injections do not improve the condition number significantly. Nevertheless, simulation results given in this study have been obtained using all four current injection profiles.

In solving equation (12) for a slice, one of the hexahedron conductivities is specified because the combined system matrix has one-less-than-full rank. Therefore, the algorithm used in this study is only appropriate to reconstruct relative (apart from a multiplicative constant) resistivity distributions. It is well known that using an additional peripheral voltage measurement is sufficient to find the absolute distribution (Kwon *et al* 2002, Khang *et al* 2002, Birgül *et al* 2003a, İder *et al* 2003).

In a real application of MREIT, one cannot measure B_z for all slices of the object. For example, if the human thorax is to be imaged, it is impractical to measure B_z for all slices from head to toe. As will be demonstrated, this may not even be necessary if the image of a certain region-of-interest (RoI) is sought for. We selected slices 23–41 which are in the middle part of the object as our RoI. We also assumed that $\nabla^2 B_z$ is known for this RoI. This means that B_z is measured only for slices 22–42, i.e. the region-of-measurement (RoM) is slices 22–42. However, for reconstruction of any slice in the RoI the combined system matrix, \mathcal{A} , must be formed which requires the calculation of current densities in that slice. Since the object is 3D, the forward solution requires the knowledge of the whole 3D resistivity distribution. For the first iteration this is not a problem but for second and subsequent iterations we have to assign a conductivity distribution to the outside of the RoI. Therefore, we assigned blurred (low pass filtered) versions of top and bottom slices of the RoI to out-of-RoI regions. For example, to fill the upper side of RoI we first placed a blurred version of the top slice of RoI as the next upper slice. Then we reblurred this slice and assigned it to the next upper slice. By this approach we assigned smoothly varying resistivity distributions to out-of-RoI regions such that as the distance of a slice from RoI increases, the resistivity distribution of that slice approaches a uniform distribution with a value equal to the mean of the resistivity distribution of the starting slice, i.e. the top (or the bottom) slice of the RoI.

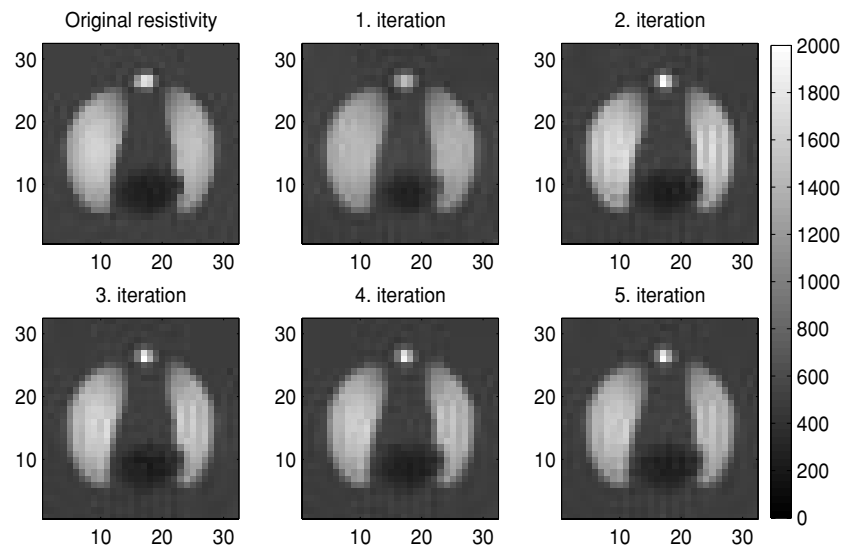


Figure 5. Five iterations of reconstructed resistivity for slice 32.

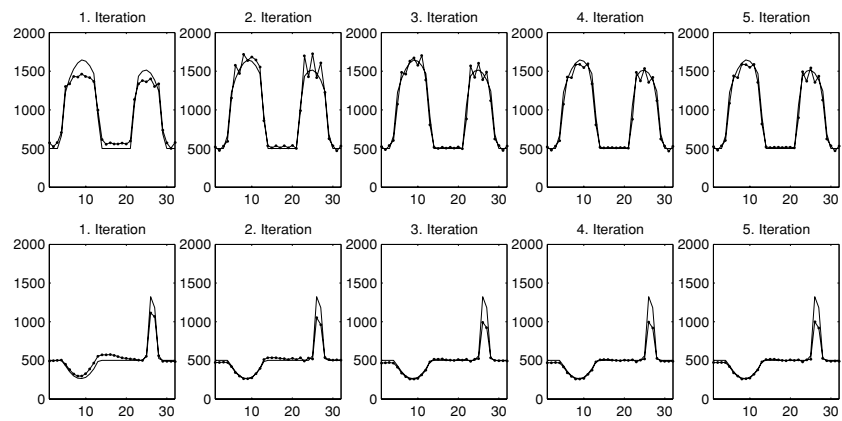


Figure 6. Five iterations of reconstructed resistivity profiles (mid- x and mid- y) for slice 32. The solid lines are the original (actual) profiles and the dotted lines are the reconstructed profiles.

The blurring filter is a 9×9 FIR filter with 0.18 cm^{-1} cut-off frequency (-3 dB), the frequency response of which is given in figure 7. With this filter six slices above (or below) the RoI, approximately uniform resistivity distributions are achieved.

Figure 5 shows the first five iterations for slice 32 (RoI = slices 23–41). It is observed that relative L^2 error is 8.4%, 7.8%, 7.6%, 7.6% and 7.4% for the first five iterations. After the fifth iteration the error remained at about 7.4%. To have more insight on the convergence behavior of the algorithm, two profiles (mid- x and mid- y) of slice 32 are shown in figure 6. As iterations proceed, the profiles fit the actual profiles much better except for high contrast small objects.

Figure 8 shows the fifth iteration images for selected slices (RoI = slices 23–41). Due to the assignment technique (with the blurring filter) used for out-of-RoI slices, these slices

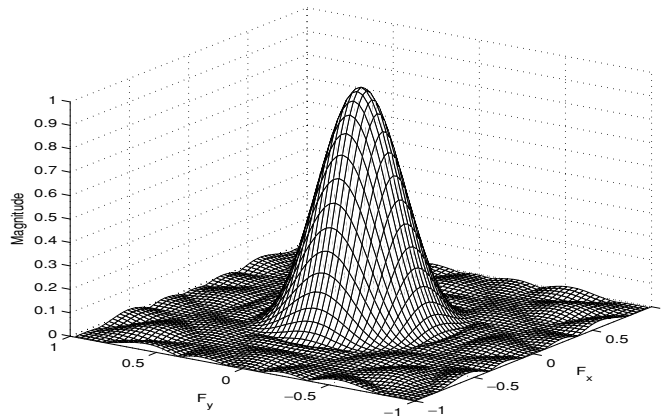


Figure 7. The blurring (low pass) filter used in assigning resistivity distributions to out-of-RoI slices. On the frequency axes, 1 corresponds to half the sampling frequency.

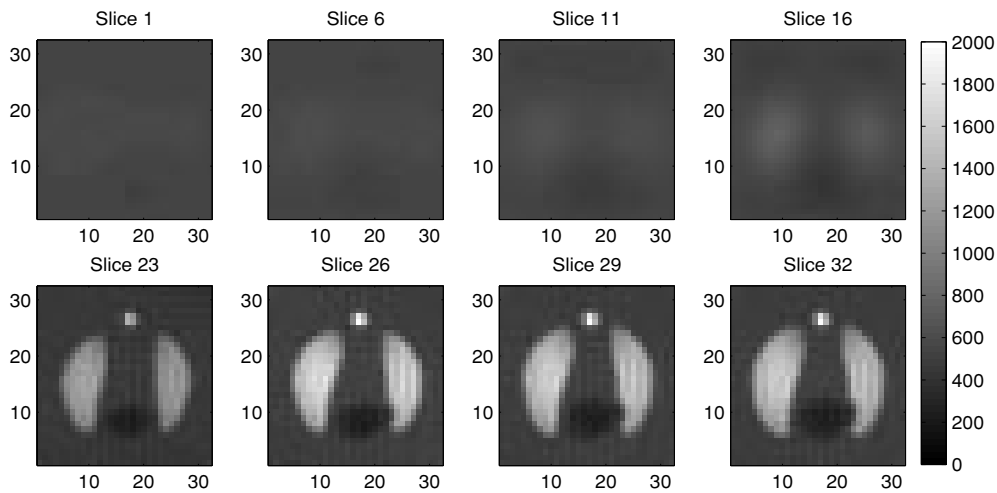


Figure 8. Fifth iteration reconstructed resistivities for selected slices of the RoI.

are not reconstructed well but the RoI slices are reconstructed with less than 10% relative L^2 error.

Noise is then added to simulated B_z data (independently for each slice) to analyze the behavior of the algorithm against noise. The noise model of Scott *et al* (1992) is used. In this model, the standard deviation of B_z noise is estimated to be $s.d. = 1/(2 * \gamma * T_c * SNR)$, where γ is the gyro-magnetic ratio (26.75×10^7 rad/(s \times T)), T_c is the duration of applied current and SNR is the signal-to-noise-ratio of the MR system. For $T_c = 48$ ms and SNR = 30, s.d. becomes 1.24 nT. We have taken the probability density of noise to be zero-mean Gaussian. Scott *et al* (1992) have derived a probability density function for phase noise in MRI images which is very close to a Gaussian for the numerical values used in this study. Since two phase images are subtracted to obtain B_z data, noise density further approaches a Gaussian. Figure 9 shows the results of noisy simulations for total applied currents of 500 mA, 1000 mA and 1500 mA for slice 32 (iteration 5, RoI = slices 23–41). Obviously with more current the

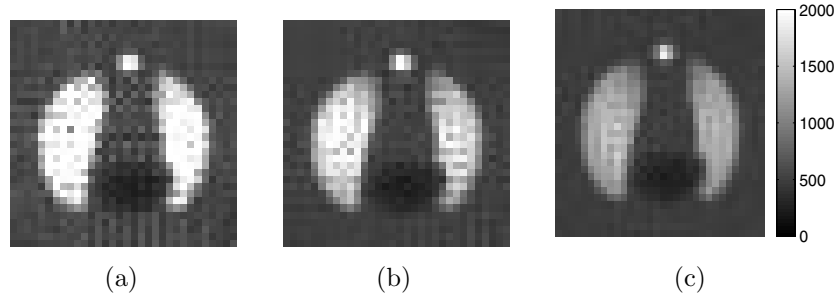


Figure 9. Fifth iteration resistivity reconstructions for slice 32 with simulated noise using total applied currents of (a) 500 mA, (b) 1000 mA and (c) 1500 mA. Relative L^2 errors for (a), (b) and (c) are 68%, 18% and 11%, respectively.

relative L^2 error is much less because in the noise model of Scott *et al* (1992), the noise in B_z does not depend on the magnitude of B_z and hence it is independent of total applied current.

Concentrating on slice 32, it is of interest to study the minimum necessary thickness for the RoI. We have chosen the RoI to encompass slices 31–34, 30–35, 29–36, 28–37, 27–38, 26–39, 25–40, 24–41 or 23–41 for which the error in the reconstructed resistivity of slice 32 is 9.7%, 9.8%, 9.7%, 9.4%, 9%, 8.8%, 8.7%, 8.4% or 7.4%, respectively. These results show that as the RoI becomes thinner, error is increased. Electrodes cover slices 22–43. For RoI thickness larger than the electrode length (in the z -direction), error still remains at around 7.4%. For slice 32 it appears that the optimum RoI is about the same thickness as the electrodes.

6. Discussion and conclusions

A new algorithm for MREIT using only one component of magnetic flux density is presented and it is demonstrated that if at least two current injection profiles are used, then acceptable (relative) images are obtained. Seo *et al* (2003b) have addressed the same problem and have published an algorithm which uses

$$\frac{\partial \sigma}{\partial x} \frac{\partial \Phi}{\partial y} - \frac{\partial \sigma}{\partial y} \frac{\partial \Phi}{\partial x} = \nabla^2 B_z / \mu_0 \quad (14)$$

instead of equation (8). It can easily be shown that equation (14) can be derived from equation (8) by a change of variables using $R = \ln(\rho)$ and $\sigma = 1/\rho$. Seo *et al* use equation (14) to iteratively find the σ distribution. At each iteration they first calculate the gradient of conductivity in a slice (using at least two current injection profiles) and then they reconstruct conductivity by integrating its gradient on straight Cartesian grid lines. Oh *et al* (2003) have followed a similar approach except that once the gradient of conductivity is found, conductivity is reconstructed using a layer potential technique. This technique appears to require accurate information about the slice boundary. The algorithm presented in this study formulates the imaging problem as a matrix equation, by which the whole R vector is solved, and therefore there is no need to develop methods for obtaining a scalar function from its gradient. One advantage of the present algorithm is that it can be easily adapted to any geometry with irregular boundary whereas integrating the gradient in an irregularly shaped object requires more effort.

In İder *et al* (2003), uniqueness and reconstruction for MREIT with known internal current density is analyzed. It is shown that if the internal current density is known then one can reconstruct resistivity using equation (4) and at least two current injection profiles. It

is also shown that there are different possibilities for numerical implementation, namely, the method of characteristics, finding and integrating the gradient and formulating reconstruction as a linear matrix equation. The only difference between the methods presented in İder *et al* (2003) and the algorithms for reconstruction from only one component of B_z is that, in the latter, the same algorithms must be applied iteratively because, since J_y and J_x in equation (8) are not known, these variables must be estimated at each iteration.

For a given slice, the system matrix for any iteration must be well conditioned. In our method, by looking at the singular value behavior of the system matrix, one can monitor the validity of the method for a given current injection profile combination. In the case of ill-conditioned matrices, the method presented in this paper can be easily modified to make use of regularization techniques such as Tikhonov regularization or truncated singular value decomposition.

An interesting observation is that even with the first iteration, one reconstructs the internal boundaries, i.e. regions where resistivity has non-zero gradient, fairly well. As iterations proceed, the numerical values of constant resistivity regions are found more accurately. One reason for having good reconstruction property for the internal boundaries is that in equation (8) the right-hand side is non-zero only at boundaries where the resistivity has non-zero gradient and even if the J_x and J_y values are not accurately known one reconstructs the boundary information well.

For the simulation object used in this study, the optimum RoI for the central slice is found to have a thickness about the same as the electrode height. This result is, of course, highly specific to the particular resistivity distribution, current injection and object geometry used in this study. In practice, one must determine the optimum RoI by making realistic simulations for the actual body sections one aims at imaging. Electrode height and width must also be experimented with together with the size of RoI.

Noisy simulations indicate that a total applied current of 1500 mA gives good reconstructions (with a relative L^2 error of 11%). With 1000 mA current, we obtained 18% error. For lower currents we did not get satisfactory results. In Lee *et al* (2003a) 28 mA is injected into a 5 cm \times 5 cm \times 5 cm phantom and satisfactory experimental results are obtained using an MRI system with SNR \simeq 30, and $T_c = 48$ mS (with relative L^2 error of 25%). In their study, denoising was used to reduce the effect of noise. In this study the object is 32 cm \times 32 cm \times 64 cm, a size much closer to thorax dimensions. Therefore, for a 32 cm \times 32 cm \times 64 cm object, roughly speaking, we need to apply around 2300 mA ($\simeq 28 \times 32 \times 64 / (5 \times 5)$) in order to have a similar amount of current density inside. Considering that we have not used any denoising in the algorithm presented in this study, and also considering that experimental studies are prone to other noise contributions not accounted for by Scott *et al*'s noise model, one may conclude that the minimum requirement for total applied current is found to be of the same order of magnitude as in Lee *et al*'s (2003) study. However, the safety limit for total current applied by electromedical instruments is 100 μ A in the frequency range of DC–1 kHz. It appears that there is still need for innovation in MREIT for decreasing the necessary amount of applied current, in addition to using advanced denoising techniques and MR machines with high SNR.

In simulations without noise, the best image obtained for slice 32 still has 7.4% relative L^2 error. Errors made in generating B_z data using the forward solver and errors made in finite difference approximations given in equations (9) and (10) contribute to the final reconstruction error. Finer meshes may be utilized to obtain more accurate results at the cost of computation time. Our forward solver for internal current density for four current injections takes about 3 min on a Pentium-4 PC with 1.7 GHz clock. One iteration of the inverse solution for all slices takes 20 min with the same PC. Generating simulated B_z data for one current injection

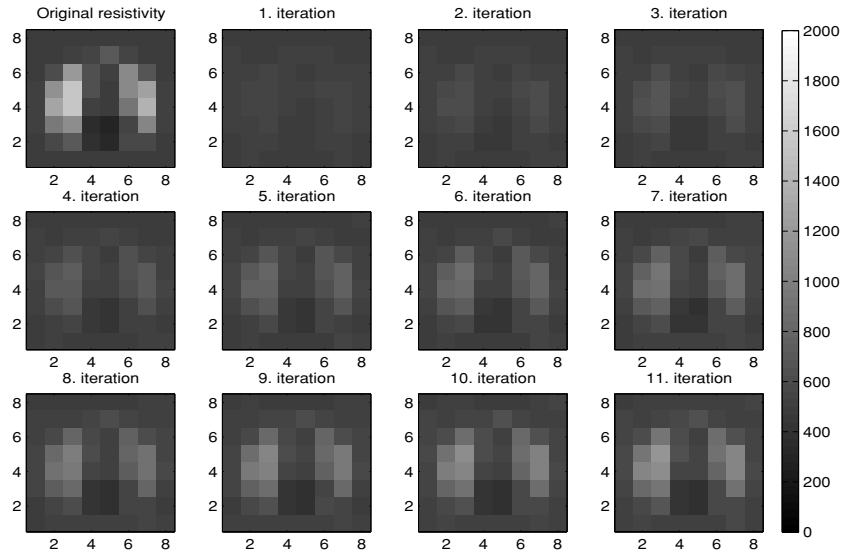


Figure 10. Slice 8 images for $16 \times 8 \times 8$ discretisation for the first 11 iterations of SMM using RoI reconstruction.

takes 2 h using optimized C-code. These computation times are formidable, and are only acceptable for feasibility studies.

In addition to algorithms which utilize $\nabla^2 B_z$ or ∇B_z there is also the sensitivity matrix method (SMM) proposed by Birgül and İder (1995), İder and Birgül (1998) and Birgül *et al* (2003b). In these earlier works, SMM is proposed for and applied to 2D simulation objects and 2D experimental phantoms. In this study 3D reconstructions are aimed at, and therefore SMM must be adapted to 3D objects.

In SMM, B_z measurements are related to conductivity perturbations using a matrix equation in the form $\Delta B_z = S \Delta \sigma$, where $\Delta B_z = B_z - B_z^0$, $\Delta \sigma = \sigma - \sigma^0$ and S is the sensitivity matrix. Here, σ^0 is the conductivity distribution around which the relation between B_z and σ is linearized, and B_z^0 is the corresponding calculated magnetic flux density. Usually σ^0 is initially considered to be uniform and the method is applied iteratively. The most straightforward adaptation to 3D is to use a sensitivity matrix which relates all B_z measurements (i.e. for all slices) to all conductivity perturbations, ending up with a huge matrix and big computational burden. To be specific, for the simulation phantom used in this study, $\Delta \sigma$ is a vector with $32 \times 32 \times 64 = 65\,536$ elements, ΔB_z is a vector with $32 \times 32 \times 64 \times 4 = 262\,144$ elements (because four current injections are used) and S is a $262\,144$ by $65\,536$ matrix. Feasible computation time and memory requirements can only be obtained by compromising spatial resolution. If the object is divided into 16 slices with 8×8 hexahedrons in each slice, it takes 30 min to complete each iteration.

It is also of interest to determine whether SMM is suitable for RoI reconstructions. For the 16 slice discretisation (i.e. $16 \times 8 \times 8$ hexahedrons), it is assumed that B_z is measured for slices 6, 7, 8, 9, 10 and $\Delta \sigma$ is taken to encompass the conductivity perturbations for these slices. Other slices are obtained by blurring as described previously. Figure 10 shows the reconstructed images for slice 8 for the first 11 iterations (after which a divergent behavior is observed). No regularization is applied and the matrix equation is solved in the least squares sense. Relative L^2 errors are 29%, 25%, 22%, 20%, 18%, 16%, 14%, 13%, 12%, 11% and 10% for the first 11 iterations. Each iteration takes 5.5 min.

This paper does not aim at investigating all aspects of SMM in relation to applying it to 3D objects. We think it suffices here to mention that although SMM appears to be behaving properly even for RoI reconstructions, it is not comparable to the algebraic method proposed in this study in terms of computation time if the same spatial resolution is requested.

Lee *et al* (2003b) have developed a 3D FEM forward solver to be used in MREIT. In their work and also in this study, where phantoms with rectangular prism blocks are used, hexahedral elements are suitable because their corners are compatible with a Cartesian grid. In the context of MREIT, a Cartesian grid is advantageous because (i) MR systems return images on an equally spaced Cartesian sampling grid and (ii) such a grid is especially handy when operators such as the Laplacian are applied to process B_z data. Lee *et al* (2003b) have used trilinear interpolation functions to approximate the potential field in a hexahedral element. Since the codes that we have developed previously are based on first-order interpolation functions, we have chosen to decompose each hexahedral element further into six tetrahedral elements. However, in order to keep the number of conductivity variables low, the conductivity distribution is discretized on a hexahedron basis, and therefore all six tetrahedrons forming a hexahedron are assigned the same conductivity value. For arbitrarily shaped realistic objects and for maximum computational efficiency, the optimum choice of FEM elements and their interpolation functions still remains to be investigated.

In a practical setting, currents in external lead wires also create a magnetic flux density within the object, and it is necessary to carefully position these lead wires to minimize the z -component of this field (Birgöl *et al* 2003b). However, within the object the Laplacian of this field is zero (Seo *et al* 2003a, Lee *et al* 2003b). The same is true for the field created by currents flowing through recessed electrodes which are proposed to minimize the effects of artifacts caused by the metallic materials of electrodes in MR images (Lee *et al* 2003b, Oh *et al* 2003). In this respect methods based on the Laplacian of B_z are preferable over other methods which utilize B_z or ∇B_z . On the other hand, amplification of noise due to twice differentiation stands as a relative disadvantage of methods using $\nabla^2 B_z$.

In Oh *et al* (2003) four electrodes are used to produce six current injection profiles. In this study eight electrodes were used to produce four current injection profiles using pairs of across electrodes in a rotating configuration. With eight electrodes one can produce $7 + 6 + 5 + 4 + 3 + 2 = 28$ profiles even when current is injected from pairs of electrodes only. However, we have shown that even with four profiles, the condition number of the combined sensitivity matrix is not improved much. In future studies, it is therefore necessary to investigate the optimum current injection strategy in relation to uniqueness and noise tolerance on one hand, and times of data acquisition and computation on the other.

References

- Birgöl Ö, Eyüboğlu B M and İder Y Z 2003a Current constrained voltage scaled reconstruction (CCVSR) algorithm for magnetic resonance- electrical impedance tomography and performance with different probing current patterns *Phys. Med. Biol.* **48** 653–71
- Birgöl Ö, Eyüboğlu B M and İder Y Z 2003b Experimental results for 2D magnetic resonance electrical impedance tomography (MR-EIT) using magnetic flux density in one direction *Phys. Med. Biol.* **48** 3485–504
- Birgöl Ö and İder Y Z 1995 Use of magnetic field generated by the internal distribution of injected currents for electrical impedance tomography *Proc. IXth Int. Conf. on Bio-Impedance* pp 418–9
- Hanselman D and Littlefield B 2001 *Mastering Matlab 6: A Comprehensive Tutorial and Reference* (Englewood Cliffs, NJ: Prentice Hall) p 321
- İder Y Z and Birgöl Ö 1998 Use of magnetic field generated by the internal distribution of injected currents for electrical impedance tomography (MR-EIT) *Elektr. Turk. J. Elec. Eng. Comput. Sci.* **6** 591–604
- İder Y Z, Onart S and Lionheart W R B 2003 Uniqueness and reconstruction in magnetic resonance–electrical impedance tomography (MR-EIT) *Physiol. Meas.* **24** 591–604

- Khang H S, Lee B I, Oh S H, Woo E J, Lee S Y, Cho M H, Kwon O, Yoon J R and Seo J K 2002 J-substitution algorithm in magnetic resonance electrical impedance tomography (MR-EIT): phantom experiments for static resistivity images *IEEE Trans. Med. Imaging* **21** 695–702
- Kwon O, Woo E J, Yoon J R and Seo J K 2002 Magnetic resonance electrical impedance tomography (mreit): simulation study of j -substitution algorithm *IEEE Trans. Biomed. Eng.* **49** 160–7
- Lee B I, Oh S H, Woo E J, Lee S Y, Cho M H, Kwon O, Seo J K and Baek W S 2003a Static resistivity image of a cubic saline phantom in magnetic resonance electrical impedance tomography (MREIT) *Physiol. Meas.* **24** 579–89
- Lee B I, Oh S H, Woo E J, Lee S Y, Cho M H, Kwon O, Seo J K, Lee J-Y and Baek W S 2003b Three-dimensional forward solver and its performance analysis for magnetic resonance electrical impedance tomography (MREIT) using recessed electrodes *Phys. Med. Biol.* **48** 1971–86
- Oh S H, Lee B I, Woo E J, Lee S Y, Cho M H, Kwon O and Seo J K 2003 Conductivity and current density image reconstruction using harmonic B_z algorithm in magnetic resonance electrical impedance tomography *Phys. Med. Biol.* **48** 3101–16
- Onart S and İder Y Z 2003 A new iterative reconstruction algorithm for MR-EIT using the Laplacian of one component of magnetic field intensity *4th Conf. on Biomedical Applications of Electrical Impedance Tomography (UMIST, Manchester, 23–25 April 2003)* p 56
- Scott G C, Joy M L G, Armstrong R L and Hankelman R M 1992 Sensitivity of magnetic resonance current density imaging *J. Magn. Reson.* **97** 235–54
- Seo J K, Kwon O, Lee B I and Woo E J 2003a Reconstruction of current density distributions in axially symmetric cylindrical sections using only one component of magnetic flux density: computer simulation study *Physiol. Meas.* **24** 565–77
- Seo J K, Yoon J-R, Woo E J and Kwon O 2003b Reconstruction of conductivity and current density images using only one component of magnetic field measurements *IEEE Trans. Biomed. Eng.* **50** 1121–4
- Silvester P P and Ferrari R L 1996 *Finite Elements for Electrical Engineers* (Cambridge: Cambridge University Press)